Electronic Supplementary Material (ESI) for Dalton Transactions.
This journal is © The Royal Society of Chemistry 2015

Electronic Supplementary Information

Elucidating the mechanism responsible for anomalous thermal expansion in a Metal-Organic Framework

Dewald P. van Heerden,[a] Catharine Esterhuysen[a]* and Leonard J. Barbour[a]*

[a] Department of Chemistry and Polymer Science, Stellenbosch University, South Africa.

Corresponding authors e-mail: ljb@sun.ac.za; ce@sun.ac.za

Contents

1 Disorder of MOF 1

The synthetic procedure of **1** ($[Zn(L)(OH)]_n$, L = 4-(1*H*-naphtho[2,3-*d*]imidazol-1-yl)benzoic acid as developed by Grobler *et al.* is summarized in Figure S1. The disorder shown for the asymmetric unit of **1·MeOH** is also present in the apohost structure.

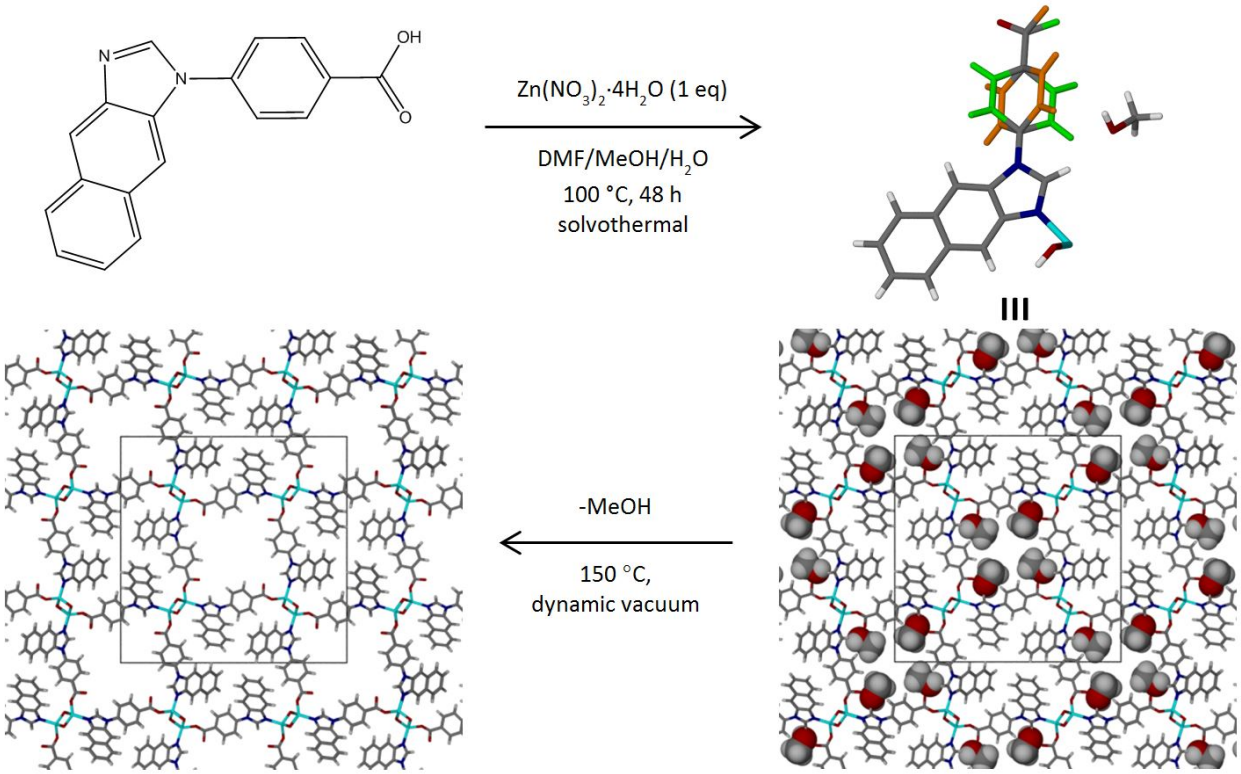

Figure S1: Synthesis of **1·MeOH** under solvothermal conditions with the asymmetric unit shown. The two positions of equal occupancy over which the benzoate moiety is disordered are shown in different colours. Desolvation under dynamic vacuum yields the apohost form, **1**.[1]

The disorder of the benzoate group persisted in the 100, 190, 280 and 370 K variable temperature single crystal X-ray diffraction structures.[1] The two positions of equal occupancy identified for the benzoate are shown in different colours in Figure S2. For computational applications, the position where the uncoordinated oxygen forms a hydrogen bond with the acidic proton of the imidazole coordinating to the same zinc atom, — in Figure S2, was retained and geometrically optimized, while the other component was omitted. This conformation was chosen to reduce crystal field effects of divergent hydrogen bonding that cannot be incorporated into a molecular representation, as opposed to the convergent hydrogen bonding across the coordination helix.

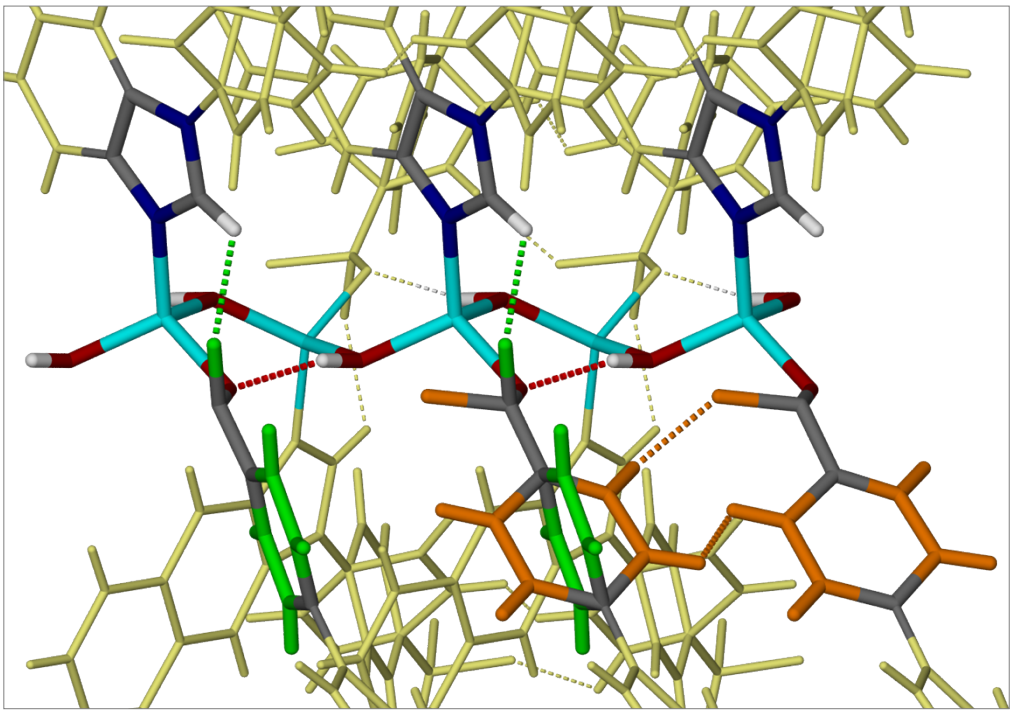

Figure S2: Depiction of two positions of equal occupancy of the disordered benzoate moiety of ligand L in compound **1**. Hydrogen bonds are shown as dashed lines. In one position (left, —), a hydrogen bond is formed with the acidic proton of the imidazole coordinating to the same zinc; in the other (right, —), hydrogen bonds are formed between neighbouring benzoate moieties.

2 Derivation of mechanistic model

The model that was developed to reproduce the proposed temperature dependent convergent expansion mechanism of the coordination helix of **1** is discussed in more detail. Rudimentary vector mathematics is employed to dictate the three dimensional movement of atoms making up a molecular representation of the coordination helix of **1** (Figure 2a of the main text).

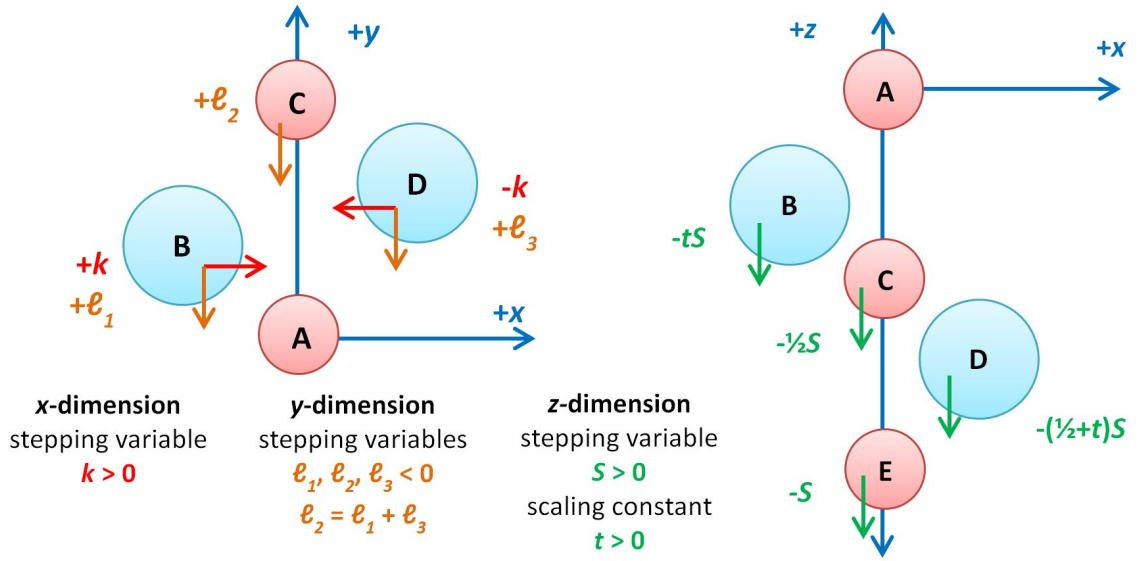

Figure S3: Depiction of the variables controlling the three-dimensional movement of atoms making up one turn of the coordination helix of **1**. A, B, C, D and E correspond to atoms O_1, Zn_2, O_3, Zn_4 and O_5, respectively.

Translation and rotation of the molecular representation onto the *z*-axis so that all O(H) *x*-coordinates become zero reduce the number of *x*-dimension variables to one since $x_A = x_C = 0$ and $x_B = -x_D$. Furthermore, in the *y*-dimension, $y_C = y_D + y_B$ and this must hold true for the duration of the simulation. As mentioned in the main text, this is due to the S_4 symmetry of the model and, after much deliberation, it was found that extension in the *z*-direction can be scaled over the five atoms making up one turn of the coordination helix by a constant (labelled t). The distance r_{AE} is equal to the *c* unit cell parameter and is stepped by variable S directly. It was therefore decided to express the movement of all atoms in terms of S, *i.e.*, to derive expressions for the changes in the *x* and *y* positions of the atoms, k and l_n, respectively, in terms of S.

In the initial model derived from the geometry-optimized 100 K crystal structure (considerations for the periodic DFT calculations are given in Section 3 below), $S = 0.0$ and the r_{AB} bond length is calculated as follows

$$r_{AB} = \sqrt{(x_B - x_A)^2 + (y_B - y_A)^2 + (z_B - z_A)^2} \qquad \{1\}$$

After incrementing *c* to $c' = c + S$, the effective r_{AB} bond length is given by

$$r_{AB}' = \sqrt{[(x_B + k) - x_A]^2 + [(y_B + l_1) - y_A]^2 + [(z_B - tS) - z_A]^2} \qquad \{2\}$$

Here, the 100 K-model Cartesian coordinates are stepped by the direction-specific stepping variables given in Figure S3. Subsequent turns are translated by an additional S in the *z* direction, but by identical translations in the *xy* plane to corresponding atoms of previous turns. The *D*-group atoms of the mechanistic model, for example, have $[x_D', y_D', z_D']$ specified by $[x_D - k, y_D + l_3, z_D - (0.5 + t)S]$ for Zn_4, $[x_D - k, y_D + l_3, z_D - (1.5 + t)S]$ for Zn_8 and $[x_D - k, y_D + l_3, z_D - (2.5 + t)S]$ for Zn_{12} (labelled according to Figure 2a and summarized in Table 2, both of the main text).

Taking the square of {2} and simplifying yields

$$\begin{aligned} r_{AB}'^2 &= (x_B + k)^2 - 2(x_B + k)x_A + x_A^2 + (y_B + l_1)^2 - 2(y_B + l_1)y_A + y_A^2 + (z_B - tS)^2 \\ &= x_B^2 + 2kx_B + k^2 - 2x_Ax_B - 2kx_A + x_A^2 + y_B^2 + 2l_1y_B + l_1^2 - 2y_Ay_B - 2l_1y_A + y_A^2 \\ &\qquad - 2z_Az_B + 2tSz_A + z_A^2 \\ &= (x_B - x_A)^2 + (y_B - y_A)^2 + (z_B - z_A)^2 + k^2 + 2k(x_B - x_A) + l_1^2 + 2l_1(y_B - y_A) \\ &= r_{AB}^2 + k^2 + 2k(x_B - x_A) + l_1^2 + 2l_1(y_B - y_A) - t^2S^2 + 2tS(z_B - z_A) \end{aligned} \qquad \{3\}$$

The boldface terms are combined to give r_{AB}^2 in the last line of {3}. Implementing the assumption that all bond lengths remain constant within the temperature range investigated, $r_{AB}' = r_{AB}$, allows equating the square of {1} and {3}to yield:

$$k^2 + 2k(x_B - x_A) + l_1^2 + 2l_1(y_B - y_A) + t^2S^2 - 2tS(z_B - z_A) = 0 \qquad \{4\}$$

Similarly, for the r_{BC} bond distance,

$$\begin{aligned} r_{BC}^{'2} = & \left[x_C - (x_B + k)\right]^2 + \left[(y_C + l_2) - (y_B + l_1)\right]^2 + \left[(z_C - 0.5S) - (z_B - tS)\right]^2 \\ = & x_C^2 - 2x_C(x_B + k) + (x_B + k)^2 + (y_C + l_2)^2 - 2(y_C + l_2)(y_B + l_1) + (y_B + l_1)^2 \\ & (z_C - 0.5S)(z_B - tS) + (z_B - tS)^2 \\ = & x_C^2 - 2x_Cx_B - 2kx_C + x_B^2 + 2kx_B + k^2 + y_C^2 + 2l_2y_C + l_2^2 - 2y_Cy_B - 2l_1y_C - 2l_2 \\ & y_B + l_1^2 + z_C^2 - Sz_C + 0.25S^2 - 2z_Cz_B + 2tSz_C + Sz_B - tS^2 + z_B^2 \quad \{5\} \\ = & (x_C - x_B)^2 + (y_C - y_B)^2 + (z_C - z_B)^2 + k^2 - 2k(x_C - x_B) + l_2^2 - 2l_1l_2 + l_1^2 + 2 \\ & (y_C - y_B) - S(z_C - z_B) + 2tS(z_C - z_B) + (0.25 - t + t^2)S^2 \\ = & r_{BC}^2 + k^2 - 2k(x_C - x_B) + (l_2 - l_1)^2 + 2(l_2 - l_1)(y_C - y_B) + (2t - 1)S(z_C - z_B) \end{aligned}$$

Again the boldface terms are combined to give r_{BC}^2 in the last line. Recognizing from Figure S3 that $l_2 - l_1 = l_3$ and implementing $r_{BC}^{'} = r_{BC}$ along with $(2t - 1) = -2(0.5 - t)$, {5} is further reduced to give

$$k^2 - 2k(x_C - x_B) + l_3^2 + 2l_3(y_C - y_B) + (0.5 - t)S\left[(0.5 - t)S - 2(z_C - z_B)\right] = 0 \quad \{6\}$$

The value of the constant t can now be obtained by substituting the values for the parameters that would render the coordination helix fully stretched out on the z axis into either {4} or {6}. This is the case when $c' = 2^{r_{AB}} + 2^{r_{BC}}$ (Table S1) and yields $t = 0.0995$. To reduce their dimensionality, these two equations are equated to obtain

$$\begin{aligned} & 2k\left[(x_B - x_A) + (x_C - x_B)\right] + l_1^2 - l_3^2 + 2l_1(y_B - y_A) - 2l_3(y_C - y_B) - 2tS\left[(z_B - z_A) + (z_C - z_B)\right] - (0.25 - t)S^2 = 0 \quad \{7\} \end{aligned}$$

Recognising that within the accuracy of the reorientation the first term in {7} is zero, an expression in terms of the y and z directions only is attained. Additionally, substituting l_3 for Yl_1, where the constant $Y = \frac{y_D}{y_B} = 10.085$, yields an expression for l_1 in terms of S:

$$(1 - Y^2)l_1^2 + 2l_1\left[(y_B - y_A) - Y(y_C - y_B)\right] - 2tS(z_C - z_A) + S(z_C - z_B) - (0.25 - t)S^2 = 0 \quad \{8\}$$

Subsequent substitution of l_1 into {4} yields a quadratic expression for k in terms of S. In both instances the $x = -\left(b + \sqrt{b^2 - 4ac}\right).(2a)^{-1}$ root was used. All the variables and, thereby, the group-specific movement of all atoms in the coordination helix are therefore dependent on the value of variable S only. For illustrative purposes, the model is depicted over the range $0\ \text{Å} \leq S \leq 2.5\ \text{Å} < S^{max}$ in Figure S4. From Figure S5 in can be seen that internal coordinates involving zinc are suitably reproduced in the mechanistic model.

Table S1: Values of variables used to solve for scaling constant t when the coordination helix is fully stretched out along the z axis.

Variable	Quantity	Value (Å)
S^{max}	$2^{r_{AB}} + 2^{r_{BC}} - \lvert z_{E,100K} \rvert$	2.5354
k^{max}	$\lvert x_{B,100K} \rvert$	0.9389

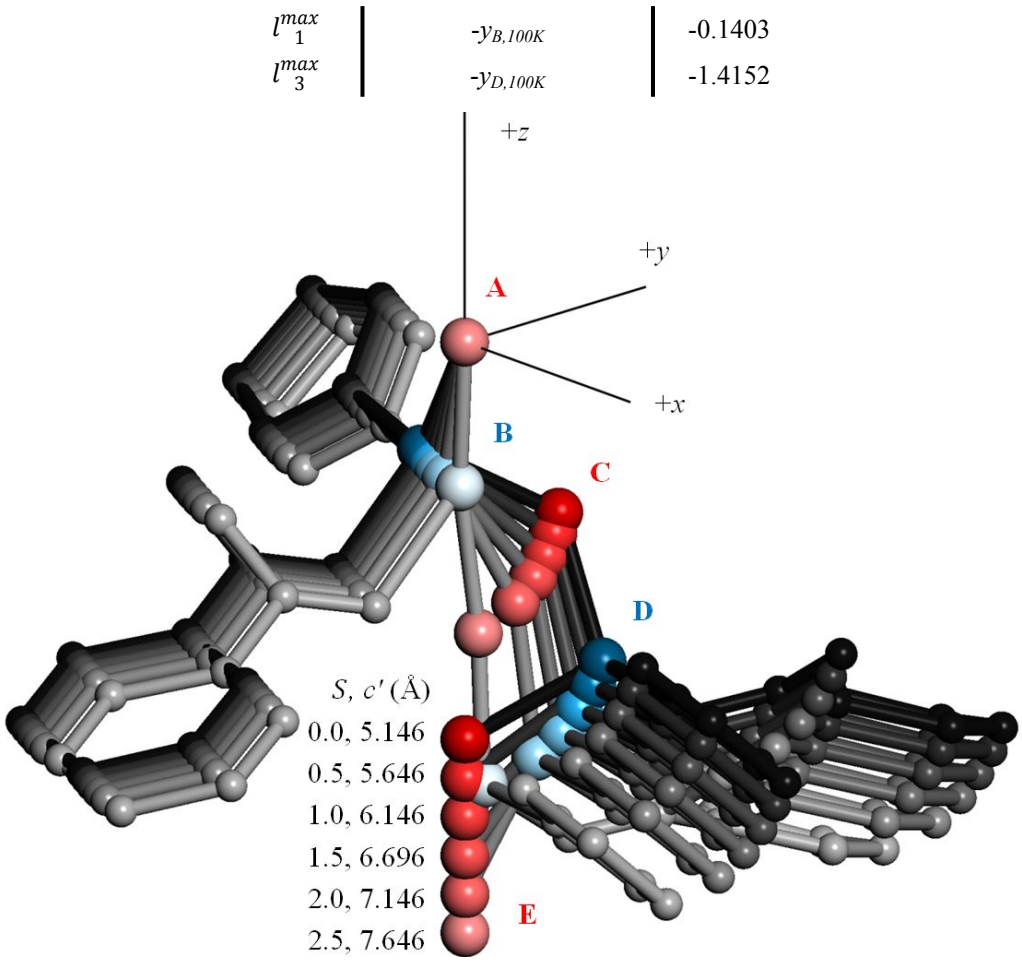

Figure S4: Overlay of the simulated model structures of one turn (atoms A to E) for values of variable S between 0.0 and 2.5 Å in 0.5 Å increments. Hydrogen atoms are omitted for clarity. Ligands are shown in grayscale while zinc atoms are coloured blue and hydroxide-oxygen atoms red. The increasing brightness gradient infers movement as S is increased. Note that the atoms A and E are stationary in the *xy* plane, while the other atoms of the coordination helix converge onto the *z* axis. The effective *c* unit cell length $^{r}_{AE} = c' = c + S$ is also shown.

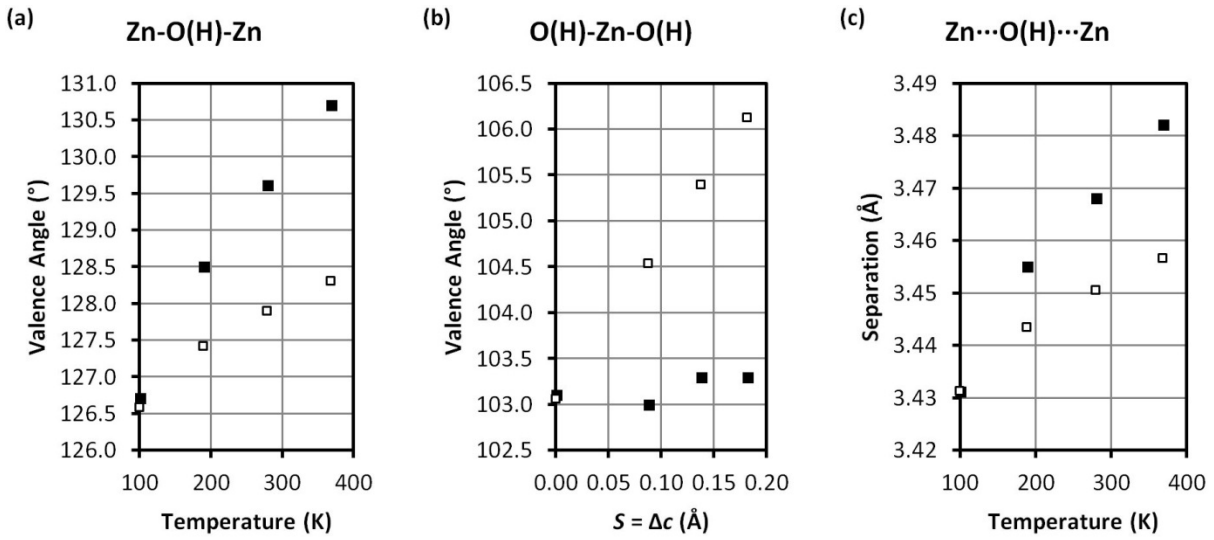

Figure S5: Comparison between internal coordinates involving zinc atoms obtained by variable temperature SCD (filled symbols) and those of the mechanistic model (open symbols). Note that the abscissas in

units of K and Å have the same variation, that is T = 100, 190, 280 and 370 K correspond to S ; 0.0, 0.09, 0.14 and 0.18 Å as calculated from the change of the *c* unit cell length relative to its value in the 100 K structure.

3 Computational Details

3.1 Molecular Dynamics simulations

Test simulations using the 2×2×2 unit cell yielded equivalent results to those found for a single unit cell, but were deemed too expensive and subsequent simulations were carried out for one unit cell. The Parrinello-Rahman barostat cell time constant was set to 1.0 ps, while the decay constant of the Berendsen thermostat was set to 0.1 ps. The Ewald summation scheme was employed for summation of nonbonded interactions. Atomic positions were optimized with the *ultra-fine* threshold values of 2.0×10^{-5} kcal mol^{-1}, 0.001 kcal mol^{-1} Å^{-1} and 1.0×10^{-5} Å for the change in energy, maximum force and maximum displacement criteria, respectively.

Simulations were carried out for 200 ps with 1 fs steps. The frame output frequency was set to 1.0 ps and the average values of the last 100 structures (second 100 ps) used to calculate average structural values for the set temperature. The first 100 ps therefore represent equilibration of the system in the NPT ensemble, with results produced in the second 100 ps.

Computed specific internal coordinates involving zinc are collected in Table S2 and comparisons to results from SCD structure elucidation (in addition to those shown in Figure 4 of the main text) are made in Figure S6.

Table S2: Computed average results for specific internal coordinates of MD simulations on one unit cell of **1** in the NPT ensemble. Greyed values are compared to those obtained by variable temperature SCD structure elucidation[1] in Figure 4 of the main text.

Temp.	Zn-O(H)-Zn		O(H)-Zn-O(H)		N-Zn-O_{carb}		Zn···L···Zn		Zn···O(H)···Zn		N-Zn-O(H)		O_{carb}-Zn-O(H)	
(K)	(°)	stdev	(°)	stdev	(°)	stdev	(Å)	stdev	(Å)	stdev	(°)	stdev	(°)	stdev
10	115.49	0.60	107.32	0.64	110.61	0.68	12.13	0.03	3.31	0.01	107.74	0.72	114.22	0.51
25	115.49	0.92	107.27	1.00	110.48	0.98	12.12	0.05	3.32	0.02	107.90	1.00	114.18	0.85
50	115.50	1.34	107.39	1.37	110.64	1.31	12.12	0.05	3.32	0.03	107.90	1.46	114.08	1.31
75	115.59	1.54	107.39	1.77	110.69	1.74	12.13	0.08	3.32	0.03	107.96	1.75	114.14	1.31
100	115.54	1.89	107.32	2.00	110.43	1.98	12.12	0.07	3.32	0.04	108.03	2.01	114.12	1.83
125	115.67	2.20	107.28	2.36	110.53	2.36	12.13	0.09	3.32	0.04	108.04	2.43	113.98	1.93
150	115.67	2.21	107.16	2.55	110.45	2.33	12.13	0.09	3.32	0.04	108.23	2.39	113.99	2.08
175	115.75	2.40	107.36	2.61	110.42	2.42	12.13	0.09	3.32	0.05	108.16	2.60	113.95	2.38
200	115.79	2.62	107.18	2.81	110.40	2.66	12.13	0.12	3.33	0.05	108.31	2.84	113.88	2.39
225	115.73	2.69	107.42	3.02	110.42	2.94	12.12	0.13	3.32	0.05	108.29	3.07	113.97	2.61
250	115.64	3.15	107.15	3.48	110.23	3.23	12.12	0.13	3.32	0.06	108.43	3.28	113.98	2.79
275	115.77	2.90	107.35	3.21	110.25	3.12	12.12	0.14	3.32	0.06	108.44	3.27	113.85	2.50
300	115.70	3.17	107.30	3.41	110.42	3.29	12.13	0.15	3.32	0.07	108.36	3.39	113.97	3.05
325	116.08	3.27	107.00	3.59	110.33	3.48	12.12	0.15	3.33	0.07	108.65	3.38	113.84	3.00
350	115.94	3.56	107.37	3.77	110.37	3.55	12.13	0.15	3.33	0.07	108.53	3.67	113.77	3.25
375	116.06	3.42	107.09	3.93	110.40	4.01	12.13	0.15	3.33	0.07	108.63	3.91	113.80	3.27
400	116.15	3.45	107.94	3.88	110.61	4.03	12.14	0.15	3.33	0.07	109.14	4.16	113.27	3.29

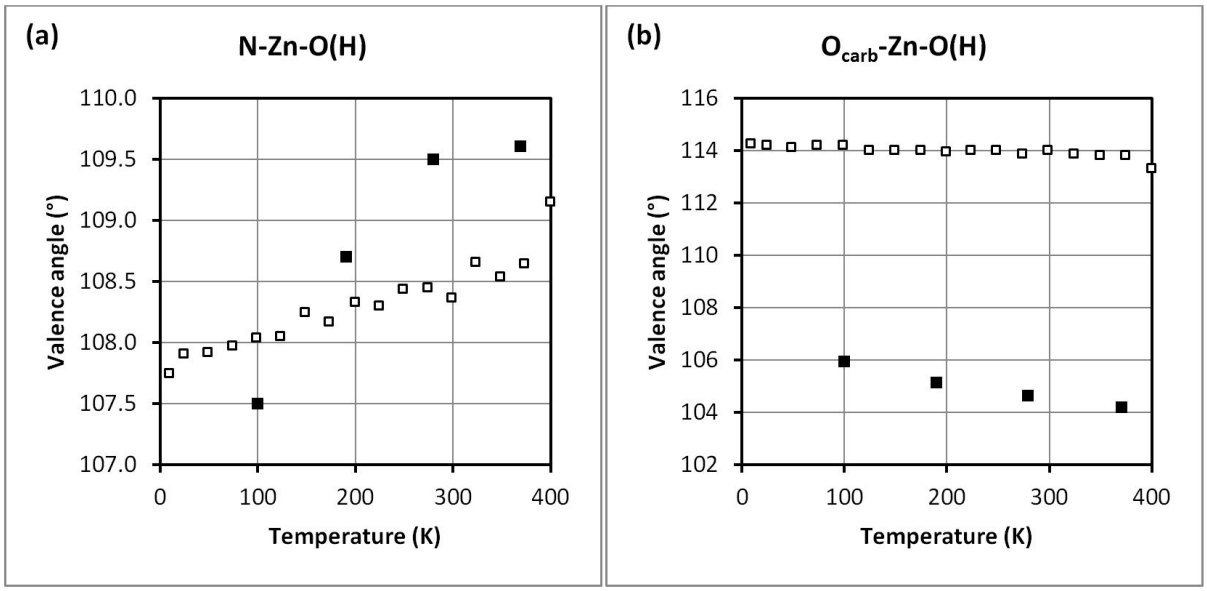

Figure S6: Comparison between internal coordinates involving zinc atoms obtained by variable temperature SCD structure elucidation (filled symbols)[1] and computed average values for MD simulations of **1** in the NPT ensemble (open symbols).

3.2 Density functionals and basis sets

The following density functionals were employed: B3LYP (hybrid GGA);[2] M06 (hybrid meta-GGA);[3] PBEPBE (pure GGA);[4] and ωB97XD (hybrid GGA).[5] All-electron basis sets considered were: 6-31G,[6] cc-PVDZ[7] and TZVP.[8] Effective core potential (ECP) basis sets comprised SDDAll,[9] where Stuttgart potentials are placed on non-hydrogen atoms, and LANL2DZ,[10] which uses Los Alamos potentials for zinc atoms. In SDDAll the D95 basis set is used for hydrogen atoms, while the D95V basis set is employed for non-zinc atoms in LANL2DZ.[11] For this study, 0 K *in vacuo* molecular calculations were carried out using the Gaussian 09 revision D.01 software package.[12] Problematic SCF-convergence and the size of the model limited the attainable density functional/basis set combinations. For example, it was necessary to specify SCF = YQC when the PBEPBE functional was used.

A model of the representation shown in Figure 2a of the main text was obtained from the optimized 100 K crystal structure (*vide infra*) and S was stepped between 0.00 and 0.20 Å in 0.05 Å increments. To solve the Schrödinger equation, a number of n-dimensional integrals need to be solved, where n depends on the method. However, the prohibitive size of systems of interest to chemists necessitates the use of numerical approximations to the analytical solutions of these integrals. Most quantum mechanics-based program packages use integration grids centred on the atoms of a system[13] according to a partitioning scheme first introduced by Becke.[14] An atom-centred integration grid is specified by (n_r,n_ℓ), where n_r is the number of radial shells per atom, and n_ℓ the number of angular points per shell. A *pruned* grid is a grid that has been optimized to achieve a given accuracy with the minimum number of grid points. For this study the pruned (99,590) grid (designated 'ultrafine' in Gaussian 09) was employed.

3.3 Dispersion correction schemes

Although DFT within the Kohn-Sham formulation[15] is, in principle, able to provide the exact ground state energy of a system, widely used density functional approximations cannot simulate the correlated motion of electrons and consequently fail when predicting dispersion-bound complexes.[16] A robust and efficient way to overcome this problem is to add an empirical atom-pairwise dispersion correction to the standard mean-field energy:[17]

$$E_{DFT-D} = E_{DFT} + E_{dispersion}$$

In the approximation that the charge distributions of the interacting species do not overlap appreciably, the dispersion potential between two ground state spherically symmetric species A and B can be expressed according to a multipole expansion approximation:[18]

$$E_{dispersion}(r_{AB}) = -\sum_{n=3,4,5,\ldots}^{\infty} \sum_{A}^{N_{at}-1} \sum_{B>A}^{N_{at}} f_{d,2n} \frac{C_{AB,2n}}{r_{AB}^{2n}}$$

where r_{AB} is the internuclear separation and the summation is over all atom pairs. The $C_{AB,2n}$ constants are dispersion coefficients where, of the leading terms, $C_{AB,6}$ describes the interaction between two instantaneous dipoles, while $C_{AB,8}$ describes the interaction between a quadrupole and a dipole. When orbital overlap is substantial, the multipole expansion is no longer valid.[19] Furthermore, in the short-range region standard density functionals already account for correlation to various extents. The multipole expansion approximation should therefore be restricted to the mid- and long-ranges to prevent *double counting* of correlation effects. A practical way to accomplish this is to incorporate a damping function, $f_{d,2n}$, into the multipolar expansion, as was first suggested by Brooks.[20]

The functional expressions for Grimme's second (GD2)[21] and third (GD3)[22] generation dispersion correction schemes are shown below along with that of Tkatchenko and Scheffler (TS):[23]

$$E_{disp}^{GD2} = -\boxed{s_6} \sum_{A}^{N_{at}-1} \sum_{B>A}^{N_{at}} \frac{C_{AB,6}}{r_{AB}^{6}} \frac{1}{1 + e^{-20(r_{AB}/r_{AB,0} - 1)}}$$

$$E_{disp}^{GD3} = -\sum_{A}^{N_{at}-1} \sum_{B>A}^{N_{at}} \left\{ \frac{C_{AB,6}}{r_{AB}^{6}\left[1 + 6\left(\frac{r_{AB}}{\boxed{s_{r,6}} r_{AB,0}}\right)^{-14}\right]} + \frac{\boxed{s_8} C_{AB,8}}{r_{AB}^{8}\left[1 + 6\left(\frac{r_{AB}}{r_{AB,0}}\right)^{-16}\right]} \right\}$$

$$E_{disp}^{TS} = -\sum_{A}^{N_{at}-1} \sum_{B>A}^{N_{at}} \frac{C_{AB,6}}{r_{AB}^{6}} \frac{1}{1 + e^{-20\left(\frac{r_{AB}}{\boxed{s_r} r_{AB,0}} - 1\right)}}$$

Those parameters that are optimized for specific density functionals are accented by boxes. The s_n values are global scaling factors, while the s_r determine the onset of the dispersion correction by scaling the cutoff radii, $r_{AB,0}$ for the interatomc distance under consideration, r_{AB}. The contribution of an atom to the dispersion interaction of a molecule depends on its chemical environment. The GD2 scheme is considered to be empirical in that atoms are assigned element specific $C_{i,6}$ coefficients regardless of their surroundings. In order to address this in GD3, Grimme and co-workers introduced the *ansatz* of a fractional coordination number and developed an elaborate geometric counting function to infer the chemical environment of an atom. In the TS scheme, on the other hand, the dispersion coefficient for an atom in a molecule is determined *ab initio* as a volumetric scale of the free-atom value, where the atom-in-molecule volume is obtained by the Hirshfeld partitioning[24] of electron density.

3.4 Mechanistic model DFT calculations

The initial atomic coordinates of the molecular representation were obtained from the geometry-optimized 100 K SCD structure. A mixed coordinate input was employed with non-hydrogen atoms specified in Cartesian coordinates and hydrogen atoms in Z-matrix notation. All hydrogen atom positions were specified in terms of the unique internal coordinates of the asymmetric unit. The symmetry of the periodic system is thereby imparted onto the molecular representationand and the number of variables reduced to 36, three internal coordinates for each of the 12 unique hydrogens. Hydrogen atom positions, including those of the truncated ligand, were optimized at the various levels of theory (a specific density functional and basis set combination) for the S = 0.0 Å model. Models for nonzero S values were subsequently generated from the optimized S = 0.0 Å models and only the hydroxide and water hydrogen atom positions (9 variables) reoptimized.

Mixed input:

```
--
 95   C   1.41   7.57   -16.98
 96   C   1.86   6.32   -16.56
 97   O   2.35   4.06   -14.95
 98   H    87    hc6     86    hcn6   85   hcnc6
 99   H    86    hc9     85    hcn9   84   hcnc9
100   H    88    hc7     87    hcn7   86   hcnc7
--
```

S = 0.0 Å

Variables:	
ho	0.975
hoZn	113.752
hoZno	-43.852
ho1	0.973
hoZn1	123.516
hoZno1	178.310
ho2	0.971
hoZn2	122.372
hoZno2	-16.229
hc1	1.087
hcc1	119.741
hccc1	176.775
hc2	1.086
hcc2	120.651
hccc2	-176.594
hc3	1.085
hcc3	120.182
hccc3	-178.628
hc4	1.082
hcc4	122.415
hccc4	177.255
hc5	1.077
hcn5	123.377
hcnc5	-175.902
hc6	1.076
hcn6	123.275
hcnc6	-181.017
hc7	1.077
hcn7	129.436
hcnc7	-181.837
hc8	1.087
hcc8	118.856
hccc8	175.752
hc9	1.006
hcn9	125.615
hcnc9	-180.744

S = 0.25 Å

Variables:	
ho	0.971
hoZn	113.159
hoZno	-43.757
ho1	0.971
hoZn1	120.404
hoZno1	184.238
ho2	0.970
hoZn2	122.205
hoZno2	-25.851
Constants:	
hc1	1.087
hcc1	119.741
hccc1	176.775
hc2	1.086
hcc2	120.651
hccc2	-176.594
hc3	1.085
hcc3	120.182
hccc3	-178.628
hc4	1.082
hcc4	122.415
hccc4	177.255
hc5	1.077
hcn5	123.377
hcnc5	-175.902
hc6	1.076
hcn6	123.275
hcnc6	-181.017
hc7	1.077
hcn7	129.436
hcnc7	-181.837
hc8	1.087
hcc8	118.856
hccc8	175.752
hc9	1.006
hcn9	125.615
hcnc9	-180.744

3.5 Periodic DFT calculations

Increased thermal motion decreased the quality of the X-ray data at higher temperatures, with hydrogen atoms poorly positioned or even absent. It was therefore decided to generate the higher temperature structures by imposing their unit cell parameters on the geometry-optimized 100 K structure and using the same fractional coordinates. Subsequent reoptimization of all atomic positions (with fixed unit cell parameters) resulted in structures that were nearly identical to those obtained from geometry optimization of each experimental structure (requiring certain atoms to be placed in chemically intuitive positions).

The positions of atoms in the crystal structures of **1** were optimized in DMol^3 employing the PBEPBE density functional augmented with GD2. Calculations were performed at the default *Fine* quality setting (important energy cut offs are listed below) of DMol^3 in Materials Studio[25] with ECP approximations and a DIIS subspace size of 6. To expedite SCF convergence, a thermal smearing parameter of 0.005 Ha was used. In thermal smearing, a fractional occupancy is assigned to one-electron states near the Fermi-level ($T = {}^{\beta}/_{k_\beta}$, with β the smearing parameter and k_β Boltzmann's constant) to allow orbitals to relax more rapidly.

SCF tolerance : 1.0×10^{-6} Ha
Numerical basis set : DNP (double numeric plus polarization): One atomic-orbital function for each occupied atomic orbital plus a second set of valence atomic orbitals augmented with a polarization d-function on all non-hydrogen atoms and a polarization p-function on all hydrogen atoms.
k-point separation : 0.07 Å^{-1}
Geometry Optimization Convergence Tolerances
Energy : 1.0×10^{-5} Ha
Maximum force : 0.002 Ha Å^{-1}
Maximum displacement : 0.05 Å

Full geometry optimizations (with fixed unit cell parameters) were carried out on the primitive cell. The conventional tetragonal unit cell comprises two lattice points positioned at (0,0,0) and (H,H,H) as shown in Figure S7. The tetragonal primitive cell is therefore half the conventional unit cell with cell parameters $a_{prim} = b_{prim} = c_{prim} = \frac{1}{2}\sqrt{2a^2 + c^2}$, $\alpha_{prim} = \beta_{prim} = \cos^{-1}\left(-c^2/(2a^2 + c^2)\right)$ and $\gamma_{prim} = \cos^{-1}\left((c^2 - 2a^2)/(2a^2 + c^2)\right)$. After atomic positions were optimized in the 100 K structure with fixed lattice parameters, the unit cell parameters of the higher temperature structures were imposed by maintaining fractional coordinates and full geometry optimizations with fixed lattice parameters subsequently carried out.

The Gaussian 09 model energy profiles shown in Figure 5 of the main text and Figure S7 (i.e. those obtained for functionals other than PBEPBE) are compared to profiles obtained for the model in DMol^3 using the same quality settings as the periodic single-point energy calculations. Single point energy values employing the PBEPBE + GD2 methodology on the DNP geometry optimized structures for different numerical basis sets are compared in Figure S10.

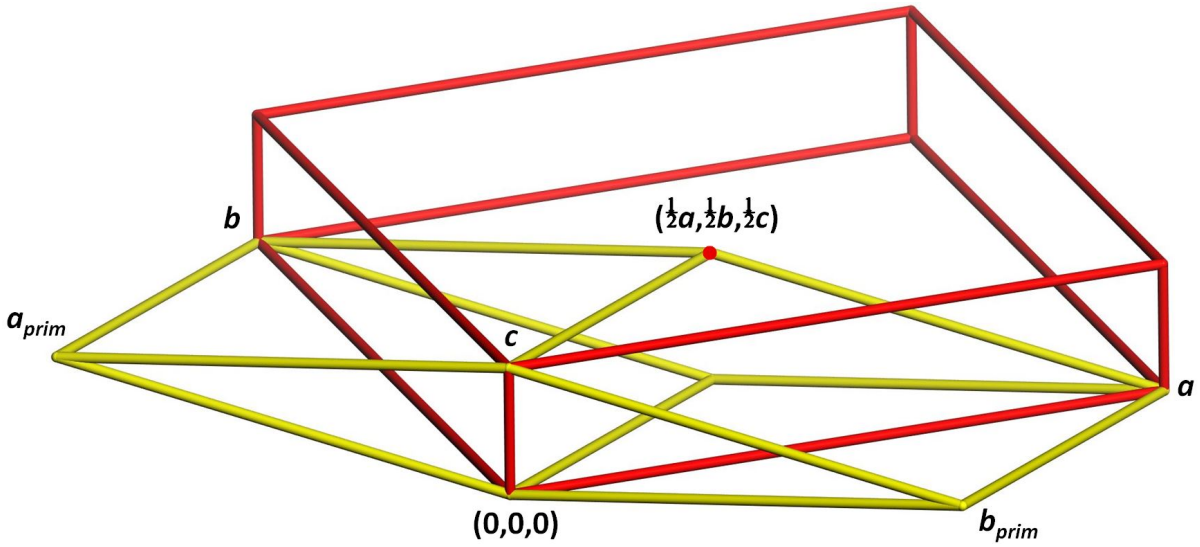

Figure S7: Overlay of the conventional and primitive tetragonal unit cells in red and yellow, respectively.

4 Additional DFT results

The DMol^3 periodic DFT single-point energy values determined using the PBEPBE density functional for one unit cell of **1** (after full geometry optimization with fixed unit cell dimension in the primitive cell) augmented by GD2 are compared to results for the TS dispersion correction scheme in Figure S8. It is clear that the results obtained with the TS correction are erratic with no clear trend perceivable, making it difficult to draw conclusions. Hence the GD2 correction is used in this study.

Results for the Gaussian 09 implemented ECP basis sets LANL2DZ and SDDAll in conjunction with the density functionals considered in the main text (*cf.* Figure 5) are also shown in Figure S8, while those obtained for the PBEPBE +GD2 methodology in conjuction with all considered GTO basis sets are shown in Figure S9. A comparison of energy profiles obtained for PBEPBE + GD2 in conjunction with different numerical basis sets from DMol^3 is also made in Figure S9. It is observed that as the size of the basis set enlarge, the steepness of the rise in energy decreases. This holds true for the all electron GTO basis sets (6-31G (1117 basis functions) > cc-PVDZ (1842) > TZVP (2299)) as well as for the numeric basis sets (MIN (577 orbitals) > DN (1045) > DNP (1716) ≈ DND (1500)), except for DNP+ (2819 orbitals). As shown in Figure S10, a similar trend is observed for periodic DFT single point energies on the PBEPBE/DNP + GD2 optimized structures.

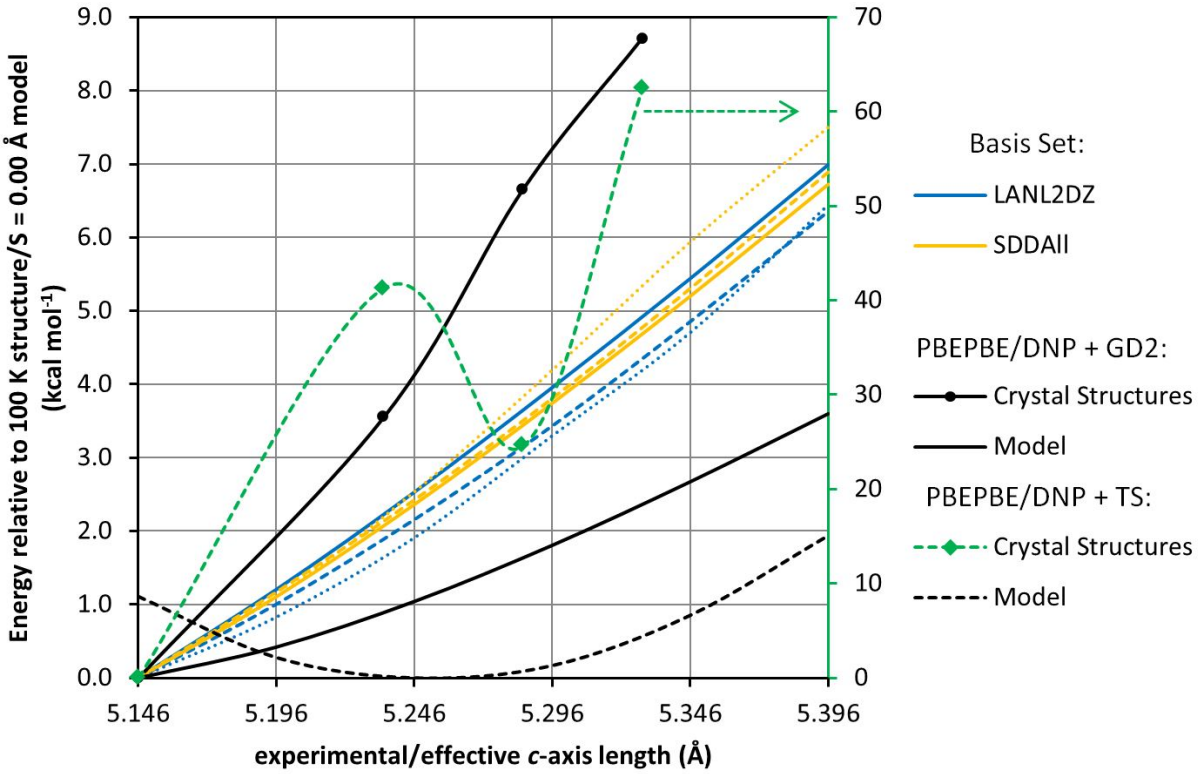

Figure S8: Comparison of single point energy values for one unit cell of **1** (solid lines with ● and dashed lines with ♦ for PBEPBE/DNP in conjunction with the GD2 and TS dispersion correction schemes, respectively) and the scaled results obtained for hydroxide (and water) hydrogen atom position optimizations of the mechanistic model: B3LYP + GD2 (—, coloured), ωB97XD (---) and M06 + GD3 (···) employing different basis sets. The right hand ordinate shows the relative energy of the PBEPBE/DNP + TS periodic DFT calculations. The variable S was stepped between 0.00 and 0.25 Å in 0.05 Å increments (yielding 5.146 Å $\leq c' \leq$ 5.396 Å). Also shown is the energy profile obtained for the model (uncoloured — and --- for PBEPBE/DNP in conjunction with GD2 and TS, respectively) in DMol^3 using the same settings as the periodic DFT single point evaluations.

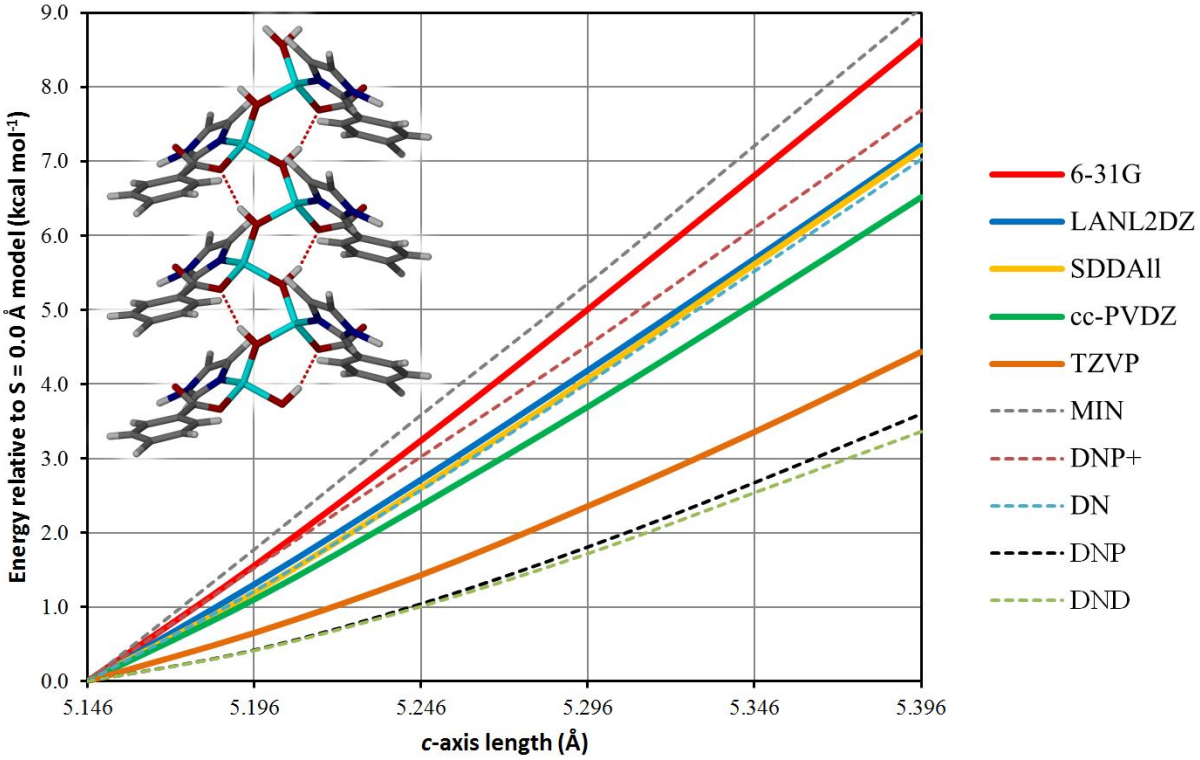

Figure S9: Comparison of relative energies obtained for the mechanistic model at the PBEPBE/basis set + GD2 level of theory as implemented in Gaussian 09 (GTO basis sets, solid lines) and DMol^3 (numeric basis sets, dashed lines).

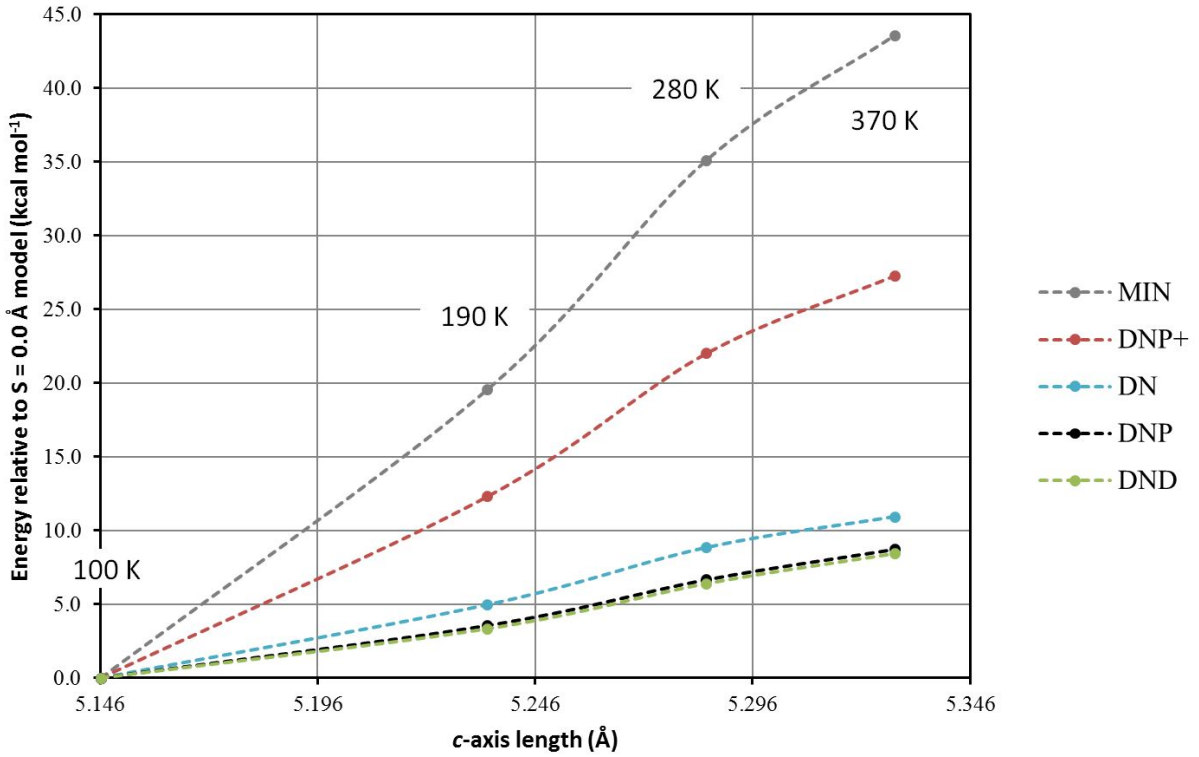

Figure S10: Comparison of relative energies obtained for the variable temperature crystal structures at the PBEPBE/basis set + GD2 level of theory as implemented in DMol^3 (numeric) for the variable temperature crystal structures.

5 Regarding the animation

The animation accompanying this publication illustrates the convergent expansion mechanism of the coordination helix extrapolated to one unit cell of **1** (*cf.* Figure S1) for the range 0.00 Å $\leq s \leq$ 2.535 Å. Hydroxide oxygen atoms are represented by pink spheres and zinc atoms by larger cyan spheres. The black dots represent the corners of the unit cell ([001] view; origin situated on the lower right corner) and the central axis of the coordination helix. On the right, the extension of three turns of the coordination helix in the *c* direction is shown. As discussed in the main text, the simultaneous change in the *a* and *b* unit cell lengths for $\Delta c = s$ is $\Delta a = \Delta b = -2k + l_2$.

6 Supplementary References

1. I. Grobler, V. J. Smith, P. M. Bhatt, S. A. Herbert and L. J. Barbour, *J. Am. Chem. Soc.*, 2013, **135**, 6411.
2. A. D. Becke, *Phys. Rev. A*, 1988, **38**, 3098; C. Lee, W. Yang and R. G. Parr, *Phys. Rev. B*, 1988, **37**, 785; B. Miehlich, A. Savin, H. Stoll and H. Preuss, *Chem. Phys. Lett.*, 1989, **157**, 200; A. D. Becke, *J. Chem. Phys.*, 1993, **98**, 5648; P. J. Stephens, F. J. Devlin, C. F. Chabalowski and M. J. Frisch, *J. Phys. Chem.*, 1994, **98**, 11623.
3. Y. Zhao and D. G. Truhlar, *Theor. Chem. Acc.*, 2008, **120**, 215.
4. J. P. Perdew, K. Burke and M. Ernzerhof, *Phys. Rev. Lett.*, 1997, **78**, 1396; J. P. Perdew, K. Burke and M. Ernzerhof, *Phys. Rev. Lett.*, 1996, **77**, 3865.
5. J.-D. Chai and M. Head-Gordon, *Phys. Chem. Chem. Phys.*, 2008, **10**, 6615.
6. W. J. Hehre, R. Ditchfield and J. A. Pople, *J. Chem. Phys.*, 1972, **56**, 2257; P. C. Hariharan and J. A. Pople, *Theor. Chim. Acta*, 1973, **28**, 213.
7. T. H. Dunning, Jr., *J. Chem. Phys.*, 1989, **90**, 1007; R. A. Kendall, T. H. Dunning, Jr. and R. J. Harrison, *J. Chem. Phys.*, 1992, **96**, 6796; D. E. Woon and T. H. Dunning, Jr., *J. Chem. Phys.*, 1993, **98**, 1358; K. A. Peterson, D. E. Woon and T. H. Dunning, Jr., *J. Chem. Phys.*, 1994, **100**, 7410; A. K. Wilson, T. van Mourik and T. H. Dunning, Jr., *J. Mol. Struct. THEOCHEM*, 1996, **388**, 339.
8. A. Schäfer, H. Horn and R. Ahlrichs, *J. Chem. Phys.*, 1992, **97**, 2571; A. Schäfer, C. Huber and R. Ahlrichs, *J. Chem. Phys.*, 1994, **100**, 5829.
9. D. Andrae, U. Haeussermann, M. Dolg, H. Stoll and H. Preuss, *Theor. Chim. Acta*, 1990, **77**, 123; A. Bergner, M. Dolg, W. Kuechle, H. Stoll and H. Preuss, *Mol. Phys.*, 1993, **80**, 1431; J. M. L. Martin and A. Sundermann, *J. Chem. Phys.*, 2001, **114**, 3408.
10. P. J. Hay and W. R. Wadt, *J. Chem. Phys.*, 1985, **82**, 299; P. J. Hay and W. R. Wadt, *J. Chem. Phys.*, 1985, **82**, 270; W. R. Wadt and P. J. Hay, *J. Chem. Phys.*, 1985, **82**, 284.
11. S. Huzinaga, *J. Chem. Phys.*, 1965, **42**, 1293; T. H. Dunning, Jr., *J. Chem. Phys.*, 1970, **53**, 2823.
12. M. J. Frisch, G. W. Trucks, H. B. Schlegel, G. E. Scuseria, M. A. Robb, J. R. Cheeseman, G. Scalmani, V. Barone, B. Mennucci, G. A. Petersson, H. Nakatsuji, M. Caricato, X. Li, H. P. Hratchian, A. F. Izmaylov, J. Bloino, G. Zheng, J. L. Sonnenberg, M. Hada, M. Ehara, K. Toyota, R. Fukuda, J. Hasegawa, M. Ishida, T. Nakajima, Y. Honda, O. Kitao, H. Nakai, T. Vreven, J. A. Montgomery Jr., J. E. Peralta, F. Ogliaro, M. Bearpark, J. J. Heyd, E. Brothers,

K. N. Kudin, V. N. Staroverov, T. Keith, R. Kobayashi, J. Normand, K. Raghavachari, A. Rendell, J. C. Burant, S. S. Iyengar, J. Tomasi, M. Cossi, N. Rega, J. M. Millam, M. Klene, J. E. Knox, J. B. Cross, V. Bakken, C. Adamo, J. Jaramillo, R. Gomperts, R. E. Stratmann, O. Yazyev, A. J. Austin, R. Cammi, C. Pomelli, J. W. Ochterski, R. L. Martin, K. Morokuma, V. G. Zakrzewski, G. A. Voth, P. Salvador, J. J. Dannenberg, S. Dapprich, A. D. Daniels, O. Farkas, J. B. Foresman, J. V. Ortiz, J. Cioslowski and D. J. Fox, *GAUSSIAN 09*, Revision D.01, Gaussian, Inc., Wallingford CT, 2013.

13. M. Malagoli and J. Baker, *J. Chem. Phys.*, 2003, **119**, 12763.
14. A. D. Becke, *J. Chem. Phys.*, 1988, **88**, 2547.
15. W. Kohn and L. J. Sham, *Phys. Rev.*, 1965, **140**, A1133.
16. E. R. Johnson, A. D. Becke, C. D. Sherrill and G. A. DiLabio, *J. Chem. Phys.*, 2009, **131**, 34111.
17. Q. Wu and W. Yang, *J. Chem. Phys.*, 2002, **116**, 515; X. Wu, M. C. Vargas, S. Nayak, V. Lotrich and G. Scoles, *J. Chem. Phys.*, 2001, **115**, 8748; U. Zimmerli, M. Parrinello and P. Koumoutsakos, *J. Chem. Phys.*, 2004, **120**, 2693.
18. R. Eisenschitz and F. London, *Z. Phys.*, 1930, **60**, 491; A. Dalgarno and W. D. Davison, *Adv. At. Mol. Phys.*, 1966, **2**, 1; A. Dalgarno, *Adv. Chem. Phys.*, 1967, **12**, 143.
19. R. J.-M. Pellenq and D. Nicholson, *Mol. Phys.*, 1998, **95**, 549.
20. F. C. Brooks, *Phys. Rev.*, 1952, **86**, 92; R. Ahlrichs, *Theor. Chim. Acta*, 1976, **41**, 7; K. T. Tang and J. P. Toennies, *J. Chem. Phys.*, 1984, **80**, 3726.
21. S. Grimme, *J. Comput. Chem.*, 2006, **27**, 1787.
22. S. Grimme, J. Antony, S. Ehrlich and H. Krieg, *J. Chem. Phys.*, 2010, **132**, 154104.
23. A. Tkatchenko and M. Scheffler, *Phys. Rev. Lett.*, 2009, **102**, 73005.
24. F. L. Hirshfeld, *Theor. Chim. Acta*, 1977, **44**, 129.
25. B. Delley, *J. Chem. Phys.*, 1990, **92**, 508; B. Delley, *J. Chem. Phys.*, 2000, **113**, 7756; *Materials Studio*, Release 7.0, Accelrys Software Inc., San Diego, USA, 2011.